Operational Forecasting Inundation Extents using REOF analysis (FIER) over Lower Mekong and Its Economic Impact on Agriculture

Chi-Hung Chang, Hyongki Lee, Son K Do, Tien Du, Kel Markert, Faisal Hossain, Shahryar Khalique Ahmad, John D. Bolten, Chinaporn Meechaiya, Hahn Chul Jung

Chi-Hung Chang

Address: Department of Civil & Environmental Engineering, University of Houston, 5000 Gulf Fwy, Bldg. 4, Rm#216, Houston, TX 77204, USA

Email: cchang37@cougarnet.uh.edu

Hyongki Lee (Corresponding Author)

Address: Department of Civil & Environmental Engineering, University of Houston, 5000 Gulf Fwy, Bldg. 4, Rm#216, Houston, TX 77204, USA

Email: hlee45@central.uh.edu

Son K Do

Address: Department of Civil & Environmental Engineering, University of Houston, 5000 Gulf Fwy, Bldg. 4, Rm#216, Houston, TX 77204, USA

Email: skdo3@cougarnet.uh.edu

Tien Du

Address: Department of Civil & Environmental Engineering, University of Houston, 5000 Gulf Fwy, Bldg. 4, Rm#216, Houston, TX 77204, USA

Email: ldu10@cougarnet.uh.edu

Kel N. Markert

Address: SERVIR Science Coordination Office, NASA Marshall Space Flight Center, Huntsville, AL 35899, USA

Email: kel.markert@nasa.gov

Faisal Hossain

Address: Department of Civil & Environmental Engineering, University of Washington, Wilcox Hall 167, 2117 Mason Rd., Seattle, WA 98195, USA

Email: fhossain@uw.edu

Shahryar Khalique Ahmad

Address: NASA/GSFC, Greenbelt, MD 20771, USA

Email: shahryarkhalique.ahmad@nasa.gov

John D. Bolten

Address: NASA/GSFC, Greenbelt, MD 20771, USA

Email: john.bolten@nasa.gov

Chinaporn Meechaiya

Address: Asian Disaster Preparedness Center, SM Tower, 24th floor, 979/69 Paholyothin Road, Samsen Nai Phayathai, Bangkok 10400, Thailand

Email: chinaporn.m@adpc.net

Hahn Chul Jung

Address: Korea Ocean Satellite Center, Korea Institute of Ocean Science & Technology, KIOST

Email: hahnchul.jung@kiost.ac.kr

Abstract

In the Lower Mekong River Basin floodplains, rice cultivation is highly crucial for regional and global economies and food security. However, prolonged flooding can pose damages to rice cultivation and other socio-economic aspects. Yet, there is no rapid operational inundation forecasting system that can help decision-makers proactively mitigate flood damages. Here, we integrated the so-called Forecasting Inundation Extents using Rotated empirical orthogonal function analysis (FIER) framework with an altimetry-based operational Mekong River level forecasting system and built an operational web application (FIER-Mekong: https://skd862-fier-mekong-demo-vlobm9.streamlitapp.com/) that generates inundation forecasts with up to 18-day lead times in about 20 seconds on daily basis with a promising skill (> 70% of critical success index). Its application to predict spatial flood-induced rice economic losses is also presented, demonstrating FIER-Mekong could have contributed to save up to 87 and 53 million US dollars during the harvest time of 2020 and 2021, respectively.

Keywords: Operational inundation forecasting, SAR imagery, flood risk prediction, Mekong River Basin

1 Introduction

In the Lower Mekong River Basin (LMRB) floodplains, including the Tonle Sap Lake Floodplains (TSLF), Cambodian Floodplains (CF), and Vietnamese Mekong Delta (VMD), inhabitants have been heavily relying on the resources gifted by the Mekong River (MR) whose flood pattern with strong seasonality has nourished the floodplain agriculture and freshwater fishery that are major supporters of the livelihoods of local inhabitants (Mekong River Commission, MRC, 2011). In particular, agriculture, especially rice cultivation, has been a foundation of national economies and stabilizes not only regional but also global food supply (Maitah et al., 2020; Matsubara et al., 2020; Okazumi et al., 2014; Triet et al., 2018). The Cambodian population has relied on rice production in the TSLF and CF for both domestic consumption and commercial export (Cramb et al., 2020). Vietnam is the fifth largest rice producer and the third rice exporter in the world (Maitah et al., 2020) with more than half of production coming from the VMD (Kien et al., 2020; Bich Tho and Umetsu, 2022). However, rice paddies are vulnerable to prolonged floodings and can die after being continuously submerged in water for days (Mekong River Commission, MRC, 2009) which may consequently lead to regional or even global scale impacts. Prolonged floodings can also pose threats to other socio-economic aspects, such as infrastructure, fertile land, and even directly threaten human lives (Horton et al., 2022; Oddo et al., 2018). Moreover, recent studies have reported an increasing flood occurrence and intensity in the LMRB floodplains under climate change (Chen et al., 2020; Try et al., 2020a, 2020b). Therefore, it is vital to rapidly predict the inundation extents to help decision-makers develop a proactive damage prevention measure in a timely manner that can mitigate flood-induced socio-economic damages.

Conventionally, hydrodynamic models based on solving one-dimensional Saint-Venant equations or two-dimensional shallow water equations have been widely used to transform discharge outputs from rainfall-runoff models to distributed inundation extents. However, these models suffer from several sources of error (Bates et al., 2014), including model structural errors and uncertainties in: (1) the model input data including the rainfall-runoff data to set the boundary and initial conditions, (2) input Digital Elevation Model (DEM) and channel bathymetry data, (3) friction coefficients to represent energy loss mechanisms, and (4) information about hydraulic structures in the reach. All these uncertainties in hydrodynamic model calibration, boundary conditions, and topographic data can significantly influence flood inundation predictions (Teng et al., 2017; Bates et al., 2014). Furthermore, the required spatial parametric inputs may not always be available (Chen et al., 2019; Leandro et al., 2014; Teng et al., 2017). In addition, they carry a heavy computational burden, especially for a high-resolution large-scale forecasting framework, that could affect forecast lead-time and accuracy. These factors were also mentioned as sources of uncertainties and errors in Dung et al. (2011) and Triet et al. (2020, 2018), which simulated inundation extents in the VMD by a one-dimensional hydrodynamic model (MIKE11) with discharges at the upstream Mekong mainstem as the upstream boundary inputs along with a spatial interpolation technique. Triet et al. (2018) also pointed out it is challenging for the two-dimensional modeling approach to be implemented in the VMD due to the computational burden and the need of highly accurate data of the dense man-made channels and infrastructure in the region.

On the other hand, a non-modeling, terrain-based approach, such as Height Above Nearest Drainage (HAND), that employs a planar approximation has also been used (Nobre et al., 2016; Zheng et al., 2018). The HAND approach normalizes the topography according to local relative heights along the drainage network. Then, a rating curve is used to transform streamflow forecasts to depths for a given river cell. Finally, flood inundation extents are determined by selecting surrounding land cells whose HAND values are less than the given water depth in the stream (Nobre et al., 2011; Teng et al., 2017). The HAND approach requires significantly less computational power than hydrodynamic models and may work well on confined floodplains with steep valleys and straight river reaches (Bates and De Roo, 2000; Wing et al., 2019). However, a recent study by Johnson et al. (2019) demonstrated that the method severely overpredicts inundation depth in regions of low relief. In addition, the HAND approach does not account for overland water flow and backwater effects caused by infrastructure and coastal flooding. With its flat terrains, especially over the CF and VMD (Balica et al., 2014), the HAND approach may not be applicable. In fact, there is currently no operational inundation extent forecasting system in the LMRB floodplains that provides a frequent (e.g., daily) forecast of inundation to the best of our knowledge. Most of the existing studies performed a scenario analysis using the hydrodynamic models, such as analyzing long-term impacts of anticipated climate change or streamflow alteration (Horton et al., 2022; Pokhrel et al., 2018; Triet et al., 2020; Try et al., 2020a, 2020b), or post-event damage assessment (Triet et al., 2018).

Recently, space-borne remote sensing, especially using the Synthetic Aperture Radar (SAR) and visible and near-infrared sensors, has emerged as a powerful tool to depict areal inundation and its variation with repeated views over extensive spatial areas (e.g., Ahamed and Bolten, 2017; Kim et al., 2017; Lee et al., 2015; Oddo et al., 2018; Smith, 1997). Chang et al. (2020), using the TSLF as a test bed, proposed a satellite imagery-based inundation extent forecasting framework that addresses the need for computationally efficient areal inundation estimation and forecasts with high temporal resolution. This framework is named Forecasting Inundation Extents using Rotated empirical orthogonal function analysis (FIER). Simply speaking, FIER forecasts inundation extents based on a correlation between historical inundation extents and hydrological data (water levels or streamflow). Once the correlation is identified, inundation extents can be forecasted with forecasted hydrological data available from an external forecasting system. Specifically, FIER decomposes multi-temporal historical satellite images into significant spatiotemporal patterns using the Rotated Empirical Orthogonal Function (REOF) analysis (Kaiser, 1958; Lorenz, 1956). The patterns are then coupled with the hydrological data by regression models. Then, the forecasted hydrological data, when available, can be used as inputs to synthesize forecasted satellite-like images, from which the corresponding forecasted inundation extents can be delineated. Consequently, FIER becomes much more computationally efficient and scalable, compared with the conventional approaches using hydrodynamic models. FIER has been successfully implemented in the TSLF (FIER-TSLF) for daily hindcast and forecast of inundation extents using a multi-temporal stack of Sentinel-1A images, daily interpolated Jason altimetry-derived TSL levels, and the climate index.

This study further extended the research of Chang et al. (2020) by: (1) implementing FIER over the entire LMRB floodplains, where the use of conventional approaches is quite challenging, by integrating it with the operationally sustainable and computationally efficient satellite altimetry-based MR water level forecasting system (Chang et al., 2019) (see Section 2.3 and the Supplementary Information); (2) developing a publicly available operational FIER web application for the LMRB floodplains, named FIER-Mekong, that can rapidly generate and visualize daily forecasted inundation extents with different lead times. The corresponding forecasted inundation depths can also be generated and visualized by utilizing the Google Earth Engine (GEE)-based Floodwater Depth Estimation Tool (FwDET-GEE) (Peter et al., 2020). The forecasted inundation extents and depths can be used for further geospatial analysis, such as conducting spatial prediction on flood-induced socio-economic damages with other land cover data. Spatial flood damage prediction can help decision-makers take proactive actions, such as disseminating timely and effective early warnings, to manage and prevent flood damages. Here, considering the aforementioned importance of rice cultivation in the LMRB floodplains, we demonstrated the application of FIER-forecasted inundation extents on spatial prediction of flood-induced rice damages. To provide users with the flexibility to use the FIER-forecasted inundation extents, the FIER-Mekong web application also allows users to export the forecasted inundation extents and depths as Geocoded TIFFs (GeoTIFFs), a widely used and supported georeferenced raster data format, that users can conveniently conduct further geospatial analysis of their interests.

The structure of this paper is as follows: Section 2 introduces the data that were used for FIER-Mekong and its application. Section 3 explains the FIER-Mekong process, skill evaluation indices, and how the early risk assessment was conducted. Section 4 describes the FIER-Mekong web application. Section 5 presents skill evaluation of FIER-forecasted inundation extents and demonstrates early assessment of flood-induced rice economic losses. The scalability of FIER framework is also discussed. Finally, Section 6 concludes the paper and discusses future scopes.

2 Data

2.1 Sentinel-1 SAR imagery

We used Sentinel-1A VV-polarized Ground Range Detection High-resolution (GRDH) intensity imagery from which the spatiotemporal patterns of the intensities have been extracted using the REOF analysis. Sentinel-1A, equipped with C-band (5.405 GHz) SAR imaging sensor, is a satellite mission under the Copernicus Earth observation program of the European Space Agency (ESA). It was launched on April 3rd, 2014, and has been consistently providing freely available imagery with a 12-day revisiting cycle. The VV-polarization was chosen considering its superior surface water mapping capability (Markert et al., 2020; Twele et al., 2016). To cover the LMRB floodplains, four frames, including Frames 23, 29, 34, and 39 of Path 26, were used (see Figure 1). We also used Sentinel-1A images to delineate inundation extents for cross-comparison with the FIER-forecasted inundation extents. Table 1 summarizes the numbers of Sentinel-1A images used with their acquisition periods.

Table 1. Usages, acquisition periods, and the corresponding numbers of Sentinel-1A images used.

Usage	**Acquisition period (YYYY-MM-DD)**	**Number of Sentinel-1A images**
Model building	2017-03-13 to 2019-12-22	85
Cross-comparison references	2020-06-01 to 2020-10-23	13
	2021-06-08 to 2021-10-30	13

We leveraged the cloud-based GEE data catalog and Application Programming Interface (API) to alleviate the computational burden of Sentinel-1A imagery retrieval and preprocessing. A GEE API-based, open-source Python application, called Hydrologic Remote Sensing Analysis for Floods (HYDRAFloods) (https://servir-mekong.github.io/hydra-floods/) was used for preprocessing, including image mosaicking, slope correction (Vollrath et al., 2020) using the Multi-Error-Removed Improved-Terrain Digital Elevation Model (MERIT DEM) (Yamazaki et al., 2017), and the Gamma-Map speckle filtering (Lope et al., 1990). The Joint Research Center (JRC)'s Global Surface Water Data was used to mask out the permanent water bodies in the Sentinel-1A images to mitigate the influence of their surface roughness change on SAR intensities, which are often caused by winds. Another GEE API-based Python package, called RESTEE (https://github.com/KMarkert/restee), was used to convert the preprocessed GEE server-side Sentinel-1A image collection to the client-side Python gridded dataset with user-defined spatial coverage and resampling resolution so it can be processed using non-GEE-based APIs and Python libraries. To build the prototype of an operational inundation forecasting system, 0.005^{o} of spatial resolution, which is equivalent to approximately 552 m, was simply set. The FIER-estimated inundation extents will also have the same spatial resolution. Both the HYDRAFloods and RESTEE are developed by NASA SERVIR Coordination Office (SCO).

The Sentinel-1A images, MERIT DEM, and JRC data were all retrieved from the GEE data catalog at no cost.

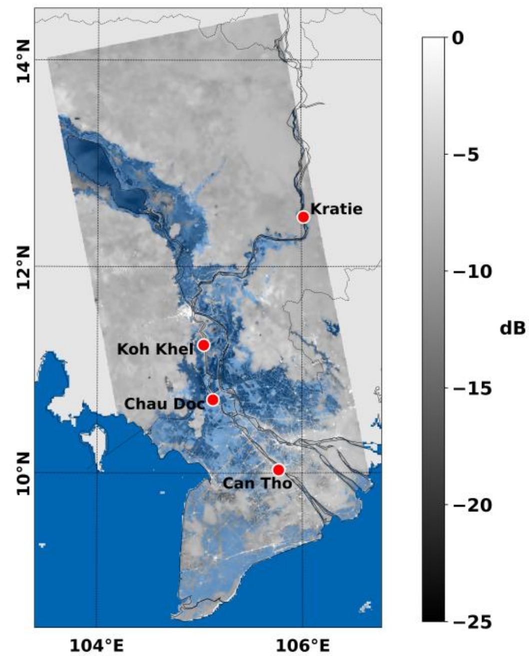

Figure 1. Sentinel-1A VV-polarized intensity image acquired on October 10th, 2018, which illustrates the spatial coverage of the imagery used. Red dots mark the gauges whose water levels were identified to be best correlated with Sentinel-1A's temporal patterns. The blue-shaded areas show the JRC historical maximum flooded areas.

2.2 MERIT DEM

The MERIT DEM (Yamazaki et al., 2017) was used for the slope correction of multi-temporal Sentinel-1A images, and as the topographic reference to derive the inundation depth maps from the inundation extents. It is a 3 arc-second-resolution global DEM with the Earth Gravitational Model 1996 (EGM96) geoid as a datum. It uses the SRTM3 DEM and the Advanced land observing satellite World 3D-30 m DEM (AW3D-30m DEM) as the baseline, where the unobserved gaps are filled by the Viewfinder Panoramas DEM. It has improved accuracy than the SRTM DEM with bias and errors being estimated and mitigated based on Ice, Cloud, and land Elevation Satellite (ICESat) laser altimetry land surface elevation data, Landsat-derived forest cover dataset (Hansen et al., 2013), and NASA global forest height data (Simard et al., 2011).

2.3 Mekong River water levels observations and forecasts

The historical in-situ water levels, provided by the MRC (https://portal.mrcmekong.org/home), were used to examine their correlation with the temporal patterns extracted from the multi-temporal Sentinel-1A images. Figure 1 shows the locations of gauges used, which are Kratie, Koh Khel, Chau Doc, and Can Tho from upstream to downstream, with red dots. Since FIER requires forecasted water levels at these gauges to generate forecasted inundation extents, the operational Variable Infiltration Capacity (VIC) model-aided satellite altimetry-based water level forecasting system (Chang et al., 2019) was used (details in Supplementary Information). Essentially, the water level forecasting system uses upstream altimetry-derived water levels to forecast the downstream water levels by assuming a linear relationship between them. This approach was adopted because (1) it is computationally efficient and thus suitable for the operational purpose; and (2) it can generate the water level forecasts with promising skills at Can Tho inside the VMD which the MRC does not routinely issue (Chang et al., 2019; Pagano, 2014). Although Chang et al. (2019) built the MR water level forecast system with up to 20-day lead time, the operational maximal lead time becomes 18-day due to the latency of input forcings of the VIC model.

2.4 Rice cover, market price, and yield

To calculate the wet season flood-induced rice economic losses, it requires the spatial distribution, market price, and the yield of rice. The rice harvest times need to be also considered. The wet season harvest time in the CF is around late August to early September (Okazumi et al., 2014). On the other hand, in the VMD, the wet season harvest time spatially varies. For double-cropping areas, the harvest time is from July to early August. For triple-cropping areas, there is an additional harvest time depending on whether the areas are fully protected or not (Triet et al., 2018). We only considered the additional harvest time of the triple-cropping areas that are not fully protected and can be vulnerable to flooding, which is from late August to early September (Triet et al., 2018). For the spatial distribution of rice paddies in the CF, the latest landcover data (for the year 2018) from the SERVIR-Mekong Regional Land Cover Monitoring System (https://www.landcovermapping.org/en/landcover/) was used. In the VMD, since the wet season harvest time spatially varies depending on local annual cropping times, the land cover data of Vu et al. (2022) (https://data.mendeley.com/datasets/kpftzmsyyz/2) was used. Both landcover data were spatially interpolated to be aligned with the inundation extents from FIER-Mekong using the nearest neighbor method.

The rice market price in US Dollar (USD)/ton was retrieved from Food and Agriculture Organization (FAO) (https://www.fao.org/markets-and-trade/commodities/rice/fao-rice-price-update/en/). The rice yield (ton/ha) was retrieved from the U.S. Department of Agriculture (USDA) (https://ipad.fas.usda.gov/countrysummary). Table 2 summarizes the retrieved data. For the rice market price, we used the average price of all rice varieties. For the rice yield, we used the average yield of the market year 2019/2020 and 2020/2021 for 2020, and the average yield of 2020/2021, and 2021/2022 for 2021.

Table 2. Rice market price and rice yield of Cambodia and Vietnam, which were used to estimate flood-induced rice economic loss.

Country	**Rice market price (USD/ton)**		**Rice yield (ton/ha)**	
	2020	**2021**	**2020**	**2021**
Cambodia	844.0	728.2	2.90	2.89
Vietnam	479.3	462.4	5.94	6.00

3 Methods

This section explains how FIER was implemented in the LMRB floodplains (FIER-Mekong). Figure 2 shows the flowchart of the entire process. FIER-Mekong was constructed using the multi-temporal Sentinel-1A intensity images and the in-situ MR water levels from MRC. With the forecasted MR water levels generated from Chang et al. (2019), the forecasted inundation extents were then produced. Then, the FIER-forecasted inundation extents were combined with the MERIT DEM to determine the forecasted two-dimensional inundation depths using the GEE-based Floodwater Depth Estimation Tool (FwDET-GEE) (Peter et al., 2020). Finally, the corresponding flood-induced rice economic losses were estimated as a demonstration of the FIER-Mekong application in preventing or mitigating the anticipated flood damages.

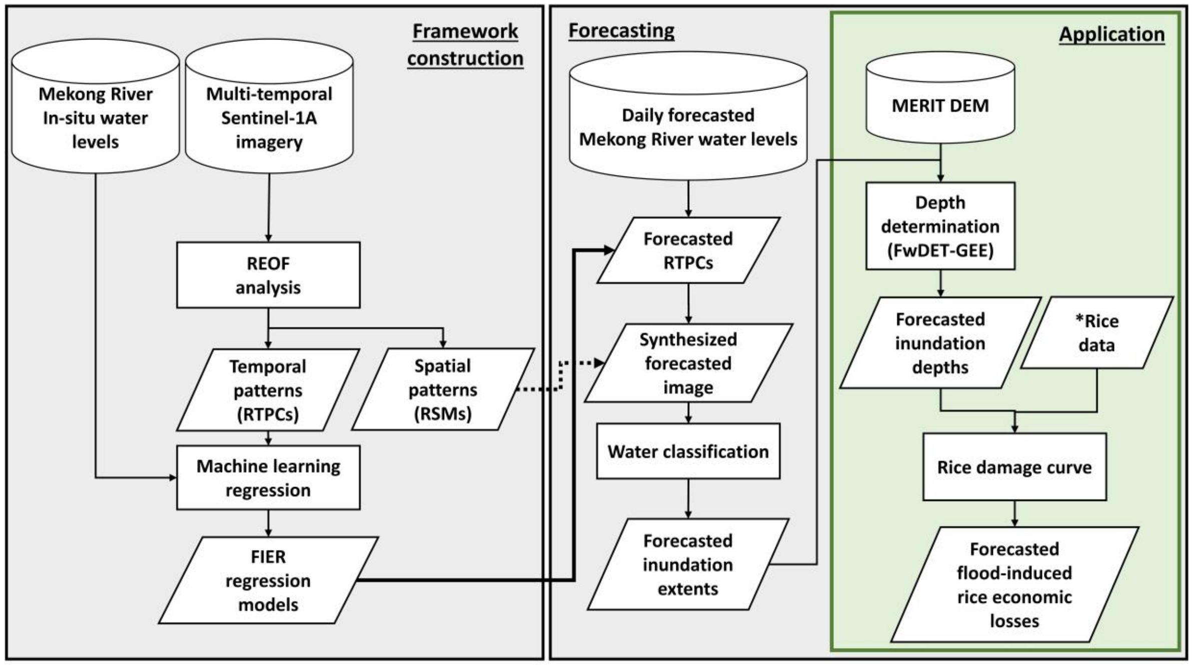

*Rice data: Rice spatial cover, market price, and yield (see Section 2.4).

Figure 2. Flowchart of FIER-Mekong, including how it was constructed, and how the forecasts were generated and applied to estimate rice economic losses.

3.1 FIER

The REOF analysis (Kaiser, 1958; Lorenz, 1956) was first applied to obtain the significant spatiotemporal patterns of multi-temporal Sentinel-1A images. Here, the first four modes of spatiotemporal patterns, accounting for about 64% of the total variance of the multi-temporal Sentinel-1A images, were identified as significant based on the Monte Carlo simulation, and were rotated to obtain the static spatial patterns, called Rotated Spatial Modes (RSMs), and the corresponding temporal patterns, called Rotated Temporal Principal Components (RTPCs). Hereafter, the first mode of RSM (RTPC) will be called RSM-01 (RTPC-01), and the second mode of RSM (RTPC) will be called RSM-02 (RTPC-02), and so forth.

A correlation analysis between the four significant modes of RTPCs and the MRC in-situ water levels was then conducted, and the four gauges whose water levels are best correlated with RTPC-01 to RTPC-04 were identified, which are Chau Doc, Koh Khel, Can Tho, and Kratie, respectively. The top panel of Figure 3 shows the RTPCs along with their best-correlated in-situ water levels and correlation coefficients (Corr.) which are all higher than 0.7 to 0.8. It means the changes in Sentinel-1A SAR intensities are temporally relevant to the water level changes at these gauges, which can be further interpreted together with the corresponding RSMs shown in the bottom panel of Figure 3. The positive correlations between the RTPCs and water levels indicate that when water levels are higher, the RTPCs will also be higher and lead to lower values after multiplying with the negative-value pixels (blue pixels) in the RSMs, which represent the floodwater occurrences. It also reflects the behavior of SAR intensities which would be lower with floodwater due to the side-looking radar imaging geometry and the specular backscattering from the water surface. By comparing with the blue-shaded areas in Figure 1, we can see that the negative-value pixels in RSMs are mostly distributed inside the floodplains.

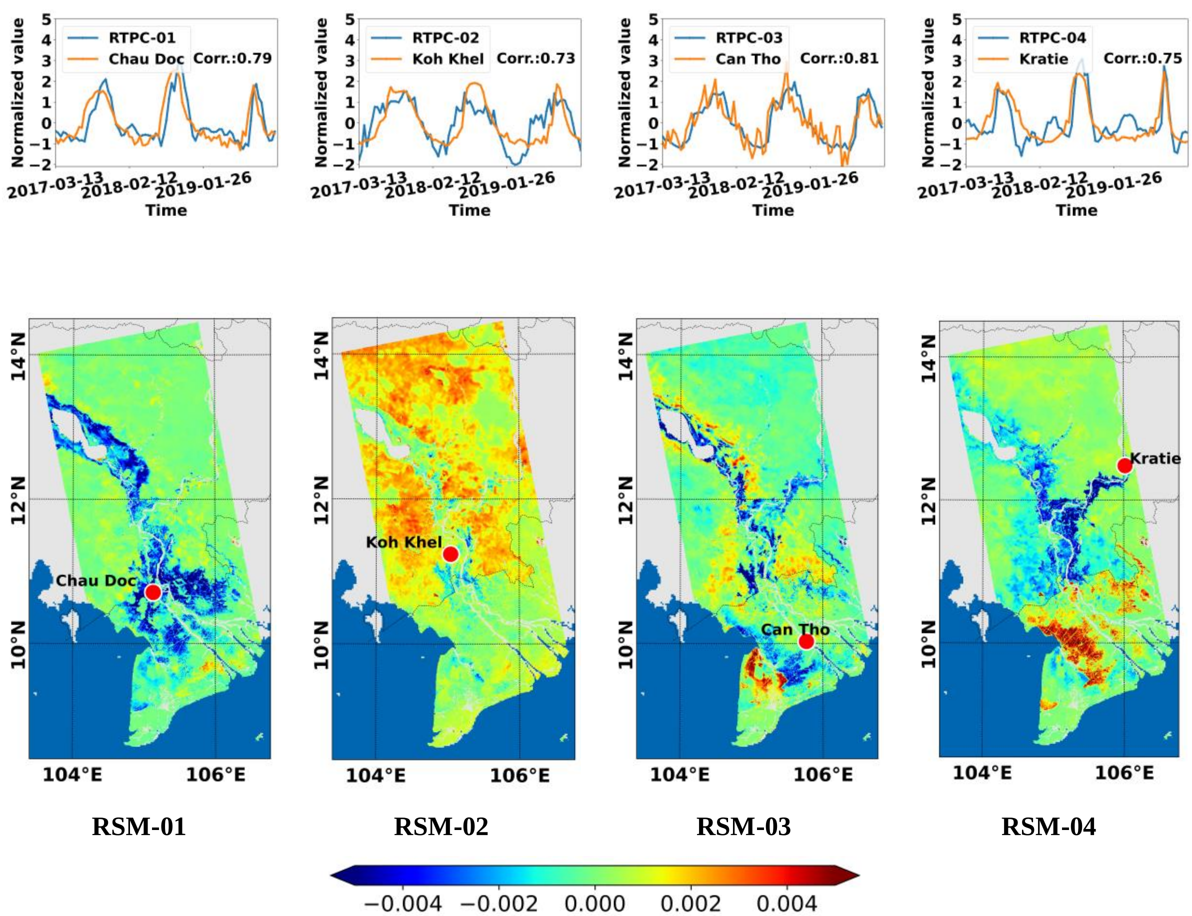

Figure 3. Significant RTPCs (top: blue), and the identified best-correlated in-situ water levels (top: orange) with correlation coefficients (Corr.), and the corresponding RSMs (bottom) where red dots mark the locations of the corresponding identified gauges.

After identifying the gauges whose water levels are best correlated with RTPCs, the neural network regression was conducted as it can provide the regression model without pre-assuming a function to be fit to the data (Imani et al., 2014). Thus, the regression models can be built without visual inspection upon the data distribution as Chang et al. (2020) did, which can help automate the FIER framework process. The optimal regression models were determined by the grid search with K-fold cross-validation approach. This approach is an automatic trial-and-error process where the training and testing are conducted using different neural network architectures and different combinations of data subsets. The data are first divided into K subsets. One of the subsets is used as a test set, while others are used as a training set. The neural network architectures in the searching space are trained until the training scores have converged and then test scores are recorded. Finally, once every subset has been used as the test set, the process ends. The optimal neural network architecture is the one that provides the best mean test score over different test sets. Such a process helps prevent the models from being overfitted (Kim et al., 2021).

The number of K is generally from 2 to 10 which could be determined based on data availability (Zhou et al., 2017). Considering the data size was 85 acquired within three years, we employed K=3 (three-fold) which ensured the test set encompassed a full hydrologic cycle (a year) of data. Both the RTPCs and MR in-situ water levels were normalized before the training, which is a common measure to expedite the training process. The Rectified Linear Unit (ReLU) activation function was adopted in the hidden layers, and the Adam gradient descent algorithm with default learning rate (0.001) was adopted as an optimizer. The mean squared error was used as the loss function to evaluate the scores. The Keras, a Python-based API with TensorFlow libraries as the backend, was used for the neural network regression process. Table 2 shows the final neural network architecture, mean training score, mean test score, and the corresponding R^2 of each mode. The R^2 were all higher than 0.6 to 0.7, considered to be satisfactory (Moriasi et al., 2007). Figure 4 shows the scatter plots of RTPCs and their corresponding water level data along with the regression models. With these regression models, the forecasted MR water levels can be fed into the models to estimate the corresponding RTPCs. Next, by summing the products of each mode of the forecasted RTPCs and RSMs, the synthesized forecasted Sentinel-1-like images can be generated.

Table 2. The optimal neural network architecture of each mode, the corresponding mean training score, mean test score, and R^2.

Mode	Number of hidden layers	Number of units per hidden layer	Mean training score	Mean test score	R^2
1	5	15	0.34	0.35	0.66
2	3	15	0.37	0.41	0.62
3	5	45	0.28	0.30	0.72
4	3	40	0.25	0.34	0.74

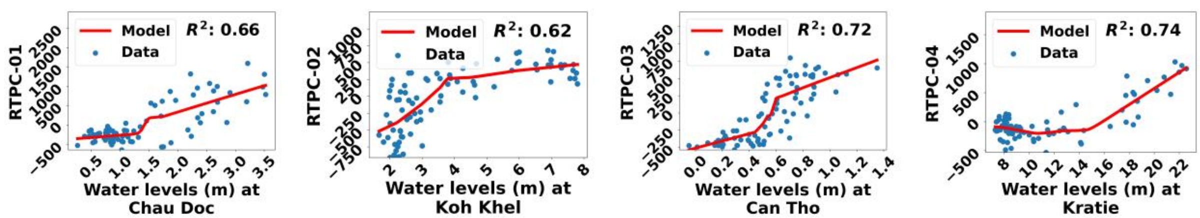

Figure 4. Scatter plots of RTPCs and their corresponding water level data along with regression models and R^2.

We applied a rapid and robust water classification method which is based on the Z-score statistics of the wet season images (DeVries et al., 2020). The method compares the change between the wet season and baseline images (representing the dry season) with the change among the baseline images using the Z-score statistics and then performs water classification. The Z-score statistics can be derived as

$$Z = \frac{\sigma_0 - \overline{\sigma_0^{baseline}}}{STD\left(\sigma_0^{baseline}\right)} \quad (1)$$

where Z is the Z-score image, σ_0 is the wet season image to be classified (FIER-synthesized or observed Sentinel-1A image), $\overline{\sigma_0^{baseline}}$, and $STD\left(\sigma_0^{baseline}\right)$ are the mean and standard deviation of the baseline images, respectively. Note that the FIER-synthesized forecasted images are the anomalies with respect to the mean of the multi-temporal Sentinel-1A images, from which the spatiotemporal patterns were extracted by the REOF analysis. Since the multi-temporal Sentinel-1A images encompass the wet season images, their mean also contains some water-related signals, and therefore was added back to the FIER-synthesized forecasted images before water classification. The baseline period was considered as the months when the monthly average in-situ water levels from 2017 to 2019 (corresponding to the acquisition period of the multi-temporal Sentinel-1A images) at the four identified gauges were the lowest. Then, the Sentinel-1A images acquired in these months were used to calculate $\overline{\sigma_0^{baseline}}$ and $STD\left(\sigma_0^{baseline}\right)$. The Z-score image was then generated and the pixels that have low Z-scores were considered to be flooded. Here, we classified the pixels whose Z-scores are lower than -3 as flooded following DeVries et al. (2020) to generate the inundation extents. The FIER-forecasted inundation extents will be cross-compared with the inundation extents derived from the real Sentinel-1A images for the skill evaluation.

3.2 Skill evaluation statistics

The skill of FIER forecasted inundation extents in the LMRB floodplains (estimation) was evaluated with pixel count-based indices including the overall accuracy, and Critical Success Index (CSI), derived from the confusion matrix (Kohavi and Provost, 1998). The inundation extents derived from real Sentinel-1A images were considered as observations. As Figure 5 illustrates, a and d are the numbers of pixels that FIER correctly estimates (true positive and true negative), respectively. Conversely, b and c are the numbers of misestimated pixels, indicating false positive and false negative, respectively.

<table>
<tr><th colspan="2" rowspan="2">Confusion Matrix</th><th colspan="2">Sentinel-1A image (Observation)</th><th rowspan="2">Marginal Total</th></tr>
<tr><th>Inundation</th><th>Non-inundation</th></tr>
<tr><td rowspan="2">FIER (Estimation)</td><td>Inundation</td><td>a
(true positive)</td><td>b
(false positive)</td><td>$a+b$</td></tr>
<tr><td>Non-inundation</td><td>c
(false negative)</td><td>d
(true negative)</td><td>$c+d$</td></tr>
<tr><td colspan="2">Marginal Total</td><td>$a+c$</td><td>$b+d$</td><td>Total =
$a+b+c+d$</td></tr>
</table>

Figure 5. Confusion matrix explaining the definition of true positive, false positive, false negative, and true negative.

The overall accuracy is the percentage of pixels that FIER correctly estimated, either true positive or true negative, over the total number of pixels:

$$\text{Overall accuracy} = \frac{a + d}{a + b + c + d} \times 100(\%). \quad (2)$$

The CSI (Gilbert, 1884), also called *threat score*, is the number of pixels that FIER correctly estimated as inundated over the number of pixels that were either estimated or observed as inundated:

$$\text{CSI} = \frac{a}{a + b + c} \times 100(\%). \quad (3)$$

The CSI avoids possible bias caused by true negative (d) (Wing et al., 2017)(Wing et al., 2017). Both overall accuracy and CSI can have a value from 0% to 100%, where 0% means there is no match between the estimation and observation, while 100% means perfect estimation.

3.3 FwDET-GEE: GEE-based inundation depth estimation

The inundation depths were determined by using the FwDET-GEE (Peter et al., 2020). The tool overlays the inundation extents on a DEM and then calculates the differences between the elevations of inundated pixels and their nearest inundated boundary pixels to estimate the inundation depths. Firstly, the inundation boundary pixels are identified, and their elevations are retrieved. Secondly, elevations of the nearest inundation boundary pixels are assigned to the non-boundary inundated pixels. Finally, the floodwater depths are estimated by subtracting the DEM value from the assigned boundary elevation at inundated pixels. Compared with the previous ArcGIS and QGIS versions, the major advantage of the GEE version is its significantly reduced processing time. The GEE script is freely accessible online (https://dataverse.harvard.edu/dataset.xhtml?persistentId=doi:10.7910/DVN/JQ4BCN). In this study, FIER-forecasted inundation extents were used as inputs to obtain the corresponding inundation depths, i.e., FIER-forecasted inundation depths, which were then used to demonstrate the application of FIER for forecasting the flood-induced rice economic loss.

3.4 Flood-induced rice economic loss estimation

To demonstrate the practical application of FIER, we estimated the flood-induced rice economic losses based on the FIER-forecasted inundation depth maps. The process starts with a rice relative damage curve, which is a function of consecutive flood duration (days) and inundation depths (m) (MRC, 2009), and has been widely used in the literature (Okazumi et al., 2014; Chung et al., 2019). In the MRC report (2009), the flood damage to rice paddies are categorized with respect to different inundation depths and duration as: (1) rice paddies will not be affected with inundation depth ≤ 0.5 m; (2) rice crops will be damaged by flood with a duration longer than 5 days; (3) rice will be completely destroyed with inundation depth ≥ 1.5 m and duration $>$ 13 days. With these, Okazumi et al. (2014) applied the damage curve with up to 13 days of flood duration, and up to 1.5 m of inundation depth as:

$$RD = (h_w - 0.5)(-86.875 + 22.5d - 0.625d^2) \tag{4}$$

where RD is rice relative damage (%), h_w is inundation depth (m) ($0.5 \leq h_w \leq 1.5$, if $h_w > 1.5$ then $h_w = 1.5$), and d is inundation duration (day) (If $d > 13$, then $d = 13$). Figure 6 shows examples of the relative damage curves. Both h_w and d can be derived from the daily FIER-forecasted inundation depth maps.

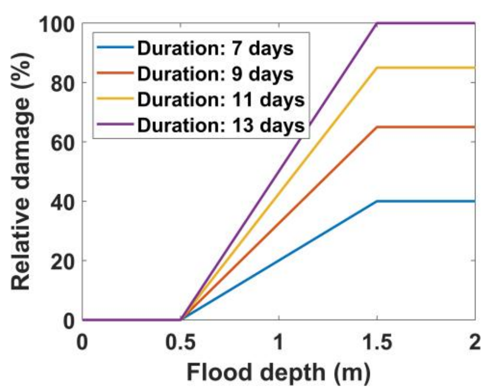

Figure 6. Rice relative damage curve (MRC, 2009).

The rice relative damages (RD) were then used to quantify the corresponding rice economic losses by

$$D = MP \times Y \times A \times \sum_{i=1}^{W} RD_i \tag{4}$$

where D is flood-induced rice damage (USD) of the country inside the Sentinel-1A image frames we used, MP is rice market price (USD/ton), Y is rice yield (ton/ha), A, and RD are area (ha) and aforementioned relative damage of a pixel, and W is the total number of pixels that represent rice under flood risk based on the aforementioned criteria in the MRC report (2009) inside the image frame for each country.

4 Operational FIER-Mekong Web Application

4.1 Configuration

The operational FIER-Mekong web application was constructed using Streamlit, an open-source Python framework that helps create, deploy, and host web applications. In Streamlit framework, a main frontend Python script that depicts the frontend elements (e.g., button, select box, calendar for the date input) along with other required libraries, and data are stored in a GitHub repository. The web application and repository are deployed and hosted by Streamlit Cloud Platform and any changes on the GitHub repository will be automatically updated.

The operational FIER-Mekong web application requires (1) automatically updated MR water level forecasts as inputs, and (2) the FIER regression models and the RSMs in the backend. As Figure 7 shows, the water level forecasts are automatically generated and then managed, stored, and updated to the Google Sheet database by using Google Sheets API and a Python library, called *pygsheets*. The automatic data updating process is executed by the Windows Task Scheduler on daily basis. The FIER regression models and the RSMs were pre-generated (see Section 3.1) and uploaded to the GitHub repository.

4.2 Graphic User Interface (GUI)

The user-friendly frontend GUI is shown in Figure 8. With the selected date of interest of up to 18 days of lead time, the corresponding forecasted water levels in the Google Sheet database will be retrieved, and the forecasted inundation extents will be visualized. There is also an option to generate and visualize the inundation depth. End-users can also choose to export the maps as GeoTIFF for further geospatial analysis.

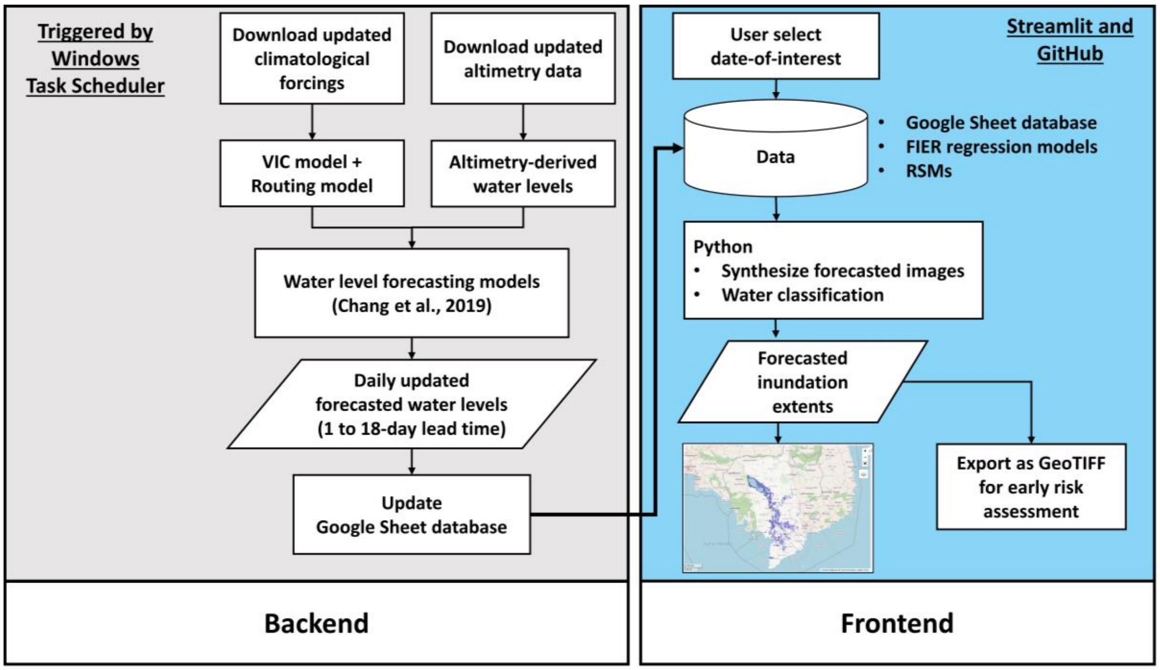

Figure 7. Configuration of the operational FIER-Mekong web application.

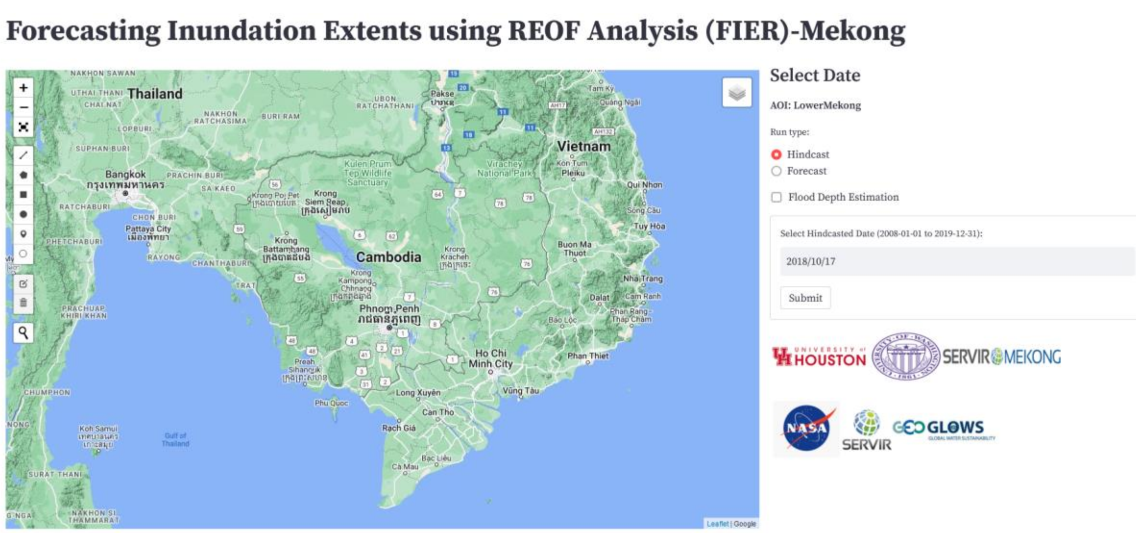

Figure 8. Frontend GUI of the operational FIER-Mekong web application (https://skd862-fier-mekong-demo-vlobm9.streamlitapp.com/).

5 Results and Discussions

5.1 Skill of FIER-forecasted inundation extents

To evaluate the skill of FIER-Mekong, we generated FIER-forecasted inundation extents with up to 18-day lead time in the wet season of 2020 and 2021 (estimation) and were cross-compared with the inundation extents directly delineated from 26 Sentinel-1A images acquired during the same period (observation) (see Table 1). The spatial resolution of inundation extents is 0.005°, equivalent to approximately 552 m (see Section 2.1). Figure 9 shows the mean and STandard Deviation (STD) of overall accuracies and CSIs of different lead times. As can be expected, the skills of FIER-forecasted inundation extents generally degrade with longer lead times. However, the mean accuracies are near 98%, and mean CSIs are about 72 to 74%, which are considered to be "fairly good" (Bernhofen et al., 2018).

The degradation of FIER inundation forecasting skills with longer lead times may be due to the errors in the forecasted water levels (see Figure 8 of Supplementary Information) which are used as an input of inundation forecasts. Since the forecasted water levels were generated based on VIC model-simulated discharges and altimetry-derived water levels at upstream Virtual Stations (VSs), errors from both of them can influence the FIER inundation forecasting skills. The potential error sources include (1) the errors of input forcing data of the VIC model, (2) the errors in the altimetry-derived water levels at upstream VSs, and (3) the assumption that there is a linear relationship between upstream and downstream water levels, ignoring the impact of tributaries and direct rainfall in between. In addition, the LMRB floodplains, specifically in the VMD, have a strong human intervention that alters the natural flood regime. Irregular human operation of water resources infrastructure (e.g., sluice gates, water pumping) in the region could affect the water levels and inundations over the floodplains (Hung et al., 2014, 2012) that cannot be predicted and consequently leads to errors in the FIER-forecasted inundation extents. The human intervention on floodplain water could also lead to uncertainties in the FIER regression models, as the models coupled the RTPCs that represent the intervened floodplain water fluctuation with the MR levels. It is, however, difficult to refine as the availability of water level observations over the floodplain is quite limited.

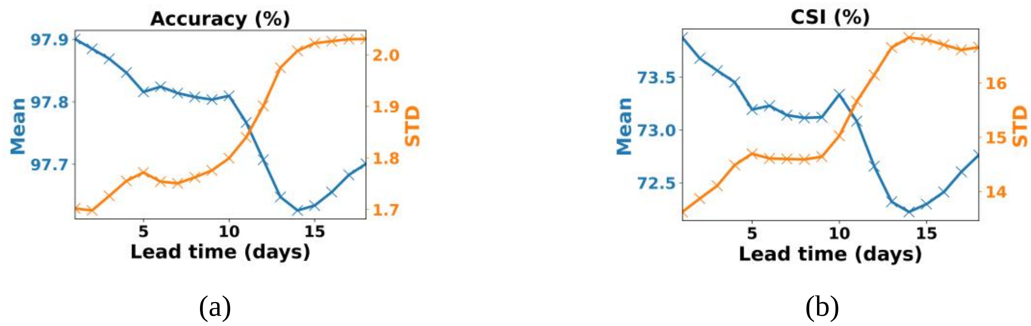

Figure 9. Mean and STD of (a) overall accuracy and (b) CSI of FIER-forecasted inundation extents in the wet seasons of 2020 and 2021.

Figure 10 shows the wet season monthly inundation occurrences (days), representing the inundation dynamics, generated using FIER-Mekong. The top and middle panels of Figure 10 illustrate the occurrences using the FIER-forecasted inundation extents (with 18-day lead time) for the wet seasons of 2020 and 2021. We start to see some inundations in August and much higher occurrences from September. In October, the inundation occurrences in the lower VMD slightly increased. The FIER-forecasted inundation extents were not large in 2020 and 2021 as they were both dry years (MRC, 2021). To demonstrate the capability of FIER-Mekong to estimate inundations in a wet year, FIER-hindcasted inundation extents for the wet season of 2018, the most recent wet year, were generated. It should be mentioned here that FIER-Mekong can also generate hindcast of inundation using the historical water levels for a date of interest obtained at the four in-situ stations (see Figure 1). The corresponding monthly inundation occurrences for the wet season of 2018 is shown at the bottom panel of Figure 10. By cross-comparing with real inundation extents derived from 11 Sentinel-1A images acquired in the 2018 wet season, the accuracy and CSI of the FIER-hindcasts are 96.6±1.9%, and 75.6±14.9%, respectively. In 2018, inundations spread out earlier than in 2020 and 2021 and were much more extensive. Some inundations started to occur in July. In August, the inundation occurrences became much higher all over the TSLF and CF. Then in October, the inundation occurrences significantly increased and widely spread over the lower VMD. The results show that FIER-Mekong is capable of generating inundation extents even for an extreme case. In other words, if the input forecasted water levels for this upcoming wet season are much higher than the ones 2020 and 2021, FIER-Mekong can be used to obtain more widespread and extreme inundations.

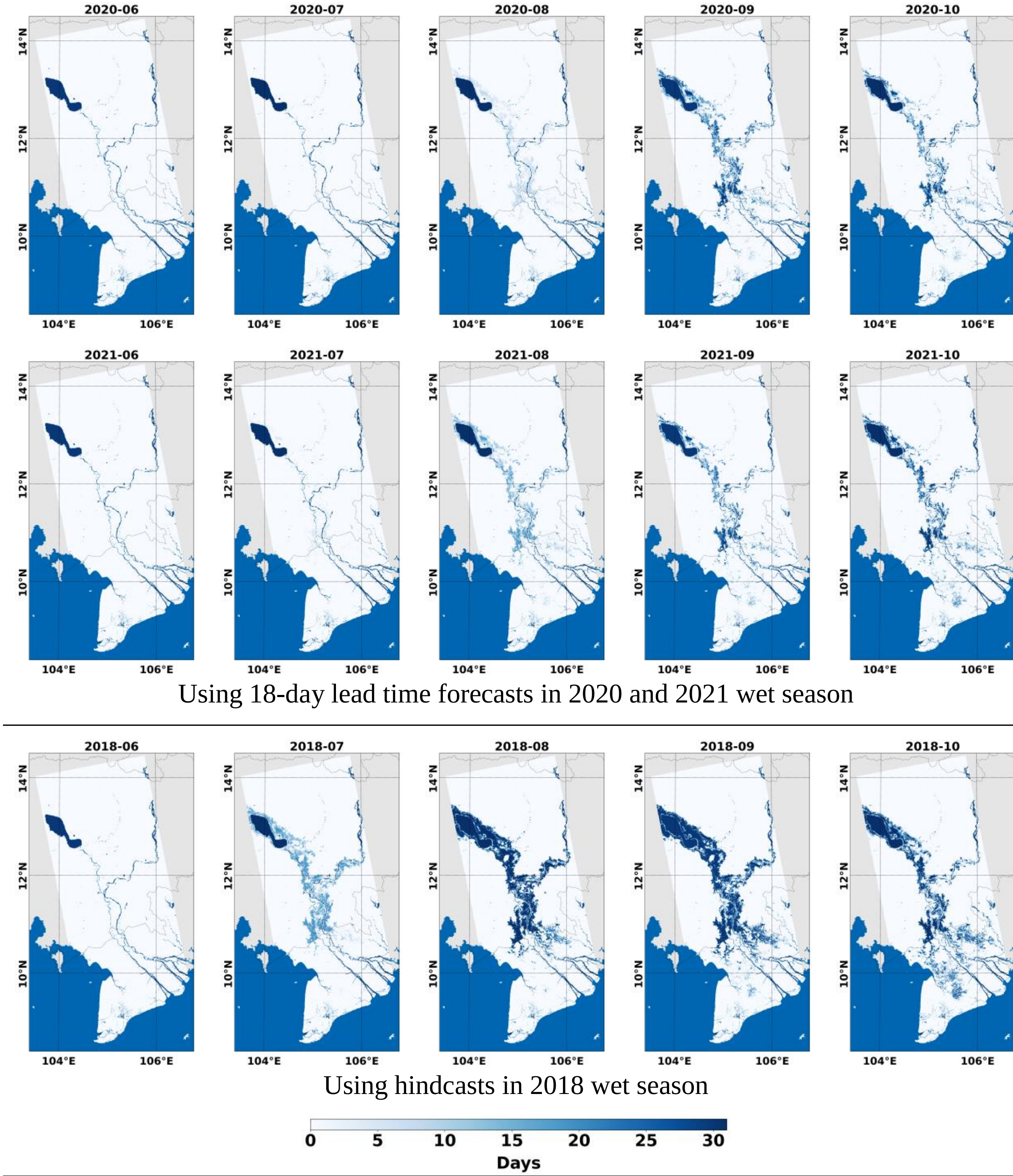

Figure 10. Monthly wet season inundation occurrences (days) generated based on (top & middle) FIER-forecasted inundation extents with 18-day lead time in 2020 and 2021 (dry years), and (bottom) FIER-hindcasted inundation extents in 2018 (wet year).

To show the locations where users can have higher confidence in the FIER-forecasted inundation extents, pixel-wise temporal correctness rates (%) were also calculated. The temporal correctness rates represent the percentage of times that each pixel was correctly estimated (either true positive or true negative) which were calculated by dividing the times that each pixel was correctly estimated by the total number of Sentinel-1A images used for the cross-comparison (26 images as Table 1 shows). To summarize the temporal correctness rates over different lead times, the mean and STD of the rates with 1-day to 18-day lead times were calculated as the top panel of Figure 11a and 11b shows, respectively. Their cumulative histograms over the pixels that have ever been estimated or observed as inundated were also generated, showing approximately 83% of pixels have mean temporal correctness rates ≥ 80% (bottom panel of Figure 11a), and about 93% of pixels have STD of temporal correctness rates ≤ 4% (bottom panel of Figure 11b). The cumulative histograms indicate that most of the pixels were correctly estimated most of the time and consistently with different lead times.

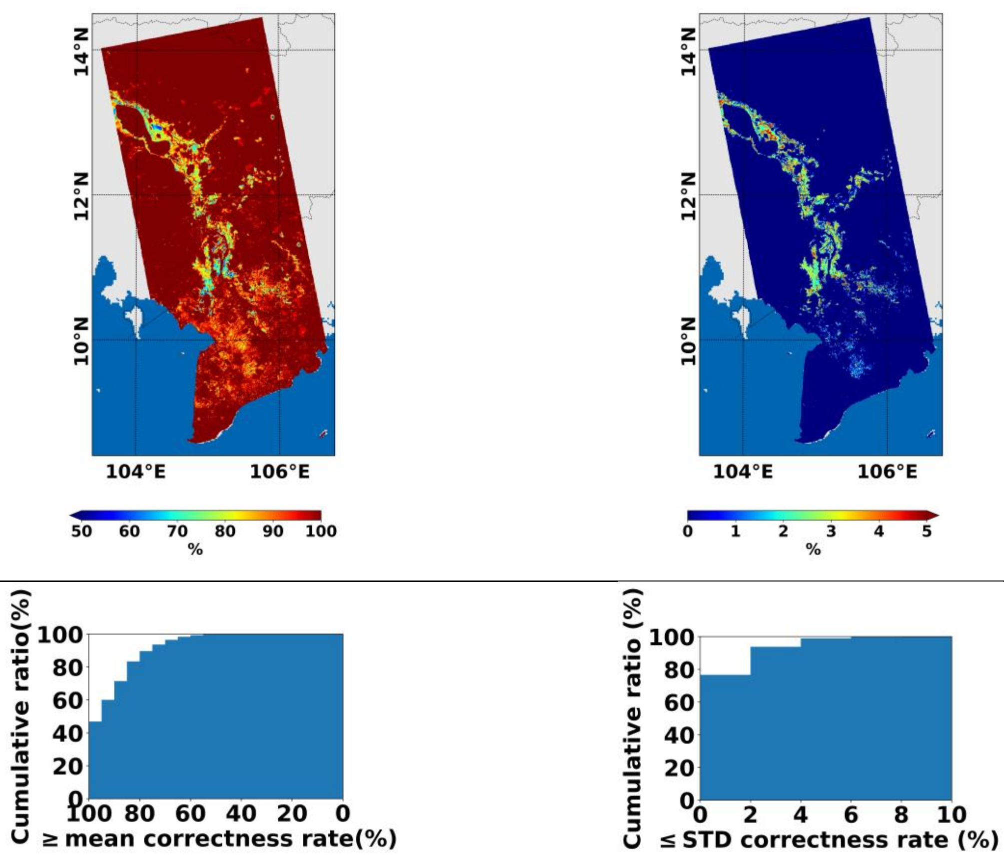

(a) (b)

Figure 11. (a) Mean, and (b) STD of temporal correctness rates of FIER-forecasts over different lead times (top panel), along with the cumulative histograms (in ratio) over the pixels that have ever been estimated or observed as inundated (bottom panel).

5.2 Application: Flood-induced rice economic losses

Floods can cause significant damages to human lives, infrastructure, and agriculture, leading to severe negative socio-economic impacts (Oddo et al., 2018). Considering the importance of rice cultivation in the LMRB to the local inhabitants and the world, we demonstrated how FIER-Mekong can be used to estimate the flood-induced rice economic losses. Since rice paddies become destroyed when they are continuously submerged under water for days, FIER can be used to rapidly forecast prolonged inundation and consequently for spatial pre-event loss prediction. Here, the FIER-forecasted inundation extents, FwDET-GEE tool (Peter et al., 2020), and the flood-induced rice relative damage curves (MRC, 2009) along with the rice data were integrated to calculate the flood-induced rice economic losses (details in Section 3.4). As a result, spatial prediction of the maximal flood-induced rice economic losses for the next 13 days was conducted for 2020 and 2021. Since 2020 and 2021 were both dry years, to show the FIER-estimated flood damages in the case of more extensive flooding, a post-event loss estimation for 2018, the most recent wet year, was also conducted based on the FIER-hindcasted inundation extents and rice data of 2018. We focused on the wet season harvest time (see Section 2.4) to calculate the losses, assuming the rice has not been reaped.

The rapid spatial predictions of flood-induced losses can give decision-makers timely information about when and where rice would be damaged along with the severity. Figure 12a shows an example of spatial predictions of flood-induced rice economic losses (in USDs) for the periods of August 29th to September 10th of 2020 (arbitrarily chosen) using the FIER-forecasts made on August 28th of 2020. The differences in flood-induced rice economic losses from place to place can be seen. Such information can help decision-makers prioritize the proactive damage prevention measures, for instance, to whom the flood risk warnings should be first disseminated. For example, this map can be used to advise farmers when and where to harvest the crops before they become damaged or destroyed due to the forthcoming flooding. Figure 13 shows the time series of FIER-forecasted flood-induced rice economic losses during the wet season harvest time of 2020 and 2021 in the CF and VMD, indicating how much rice paddies under flood risk could have been saved (in million USD) if the farmers had taken early actions based on outputs from FIER-Mekong. The maximal flood-induced rice economic losses that could have been saved with FIER-Mekong were about 86 and 52 million USD in Cambodia, and 1.5 and 1.2 million USD in Vietnam during the 2020 and 2021 wet season harvest time, respectively. The estimated losses in Vietnam were much lower than those in Cambodia probably because the Vietnamese farmers have adjusted the rice planting and harvesting calendar to the time before the arrival of main floodings (Triet et al., 2018). In addition, the VMD has a dense network of flood protection infrastructure (Hung et al., 2014, 2012). During the time of main floodings, the farmers do rice planting over fully protected areas (Triet et al., 2018) which we did not take into account when estimating the losses.

Figure 12b shows the FIER-based post-event estimation of maximal flood-induced rice economic losses during the wet season harvest time of 2018. We can observe that the largest losses occurred in the CF near the Cambodia-Vietnam national border. The post-event flood-induced loss estimation can be used as a reference for flood risk mapping and future land-use planning by public administrators or insurance companies (Oddo et al., 2018). For example, the public administrators may consider reinforcing the flood prevention infrastructures (e.g., dikes or levees), adjusting the rice planting and harvesting calendar, or planting more flood-resistant rice varieties in the areas. The insurance companies can also prioritize to whom they should market and provide flood insurance. The maximal total flood-induced rice economic losses were about 316 and 46 million USD in Cambodia and Vietnam, respectively, during the wet season harvest time of 2018.

Forecasted maximal rice economic losses
2020-08-29 to 2020-09-10

Hindcasted maximal rice economic losses
2018 wet season harvest time

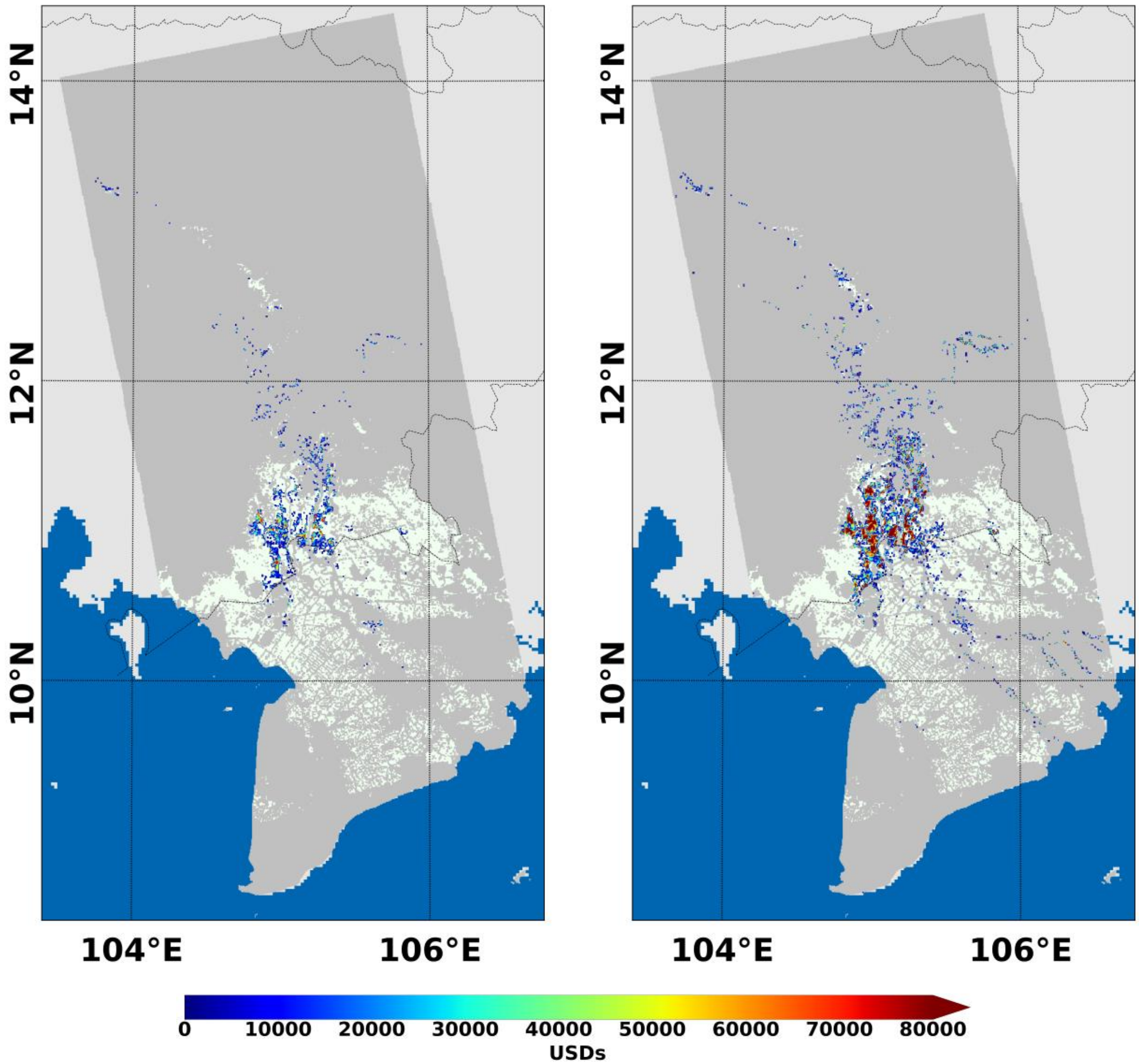

(a) (b)

Figure 12. (a) FIER-based spatial prediction of maximal flood-induced rice economic losses in the next 13 days (August 29th to September 10th of 2020 as an arbitrarily chosen example), and (b) FIER-based post-event spatial estimation of maximal flood-induced rice economic losses during the wet season harvest time of 2018. Light green pixels in the background represent the rice paddies.

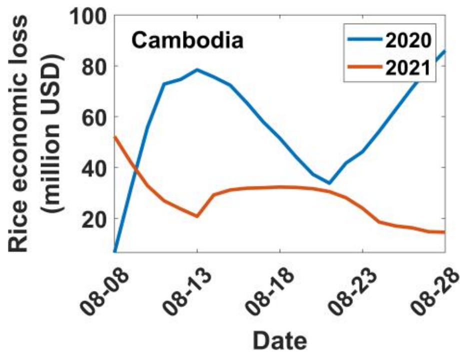

(a)

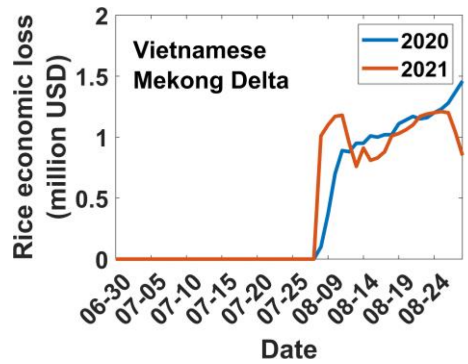

(b)

Figure 13. Daily FIER-forecasted flood-induced rice economic losses within the next 13 days during the 2020 and 2021 wet season harvest time in (a) Cambodia, and (b) the VMD inside the Sentinel-1A image frames, assuming the rice has not been reaped.

It is, however, challenging to numerically compare the estimated losses with government or agency statistics, as they are often reported from different data sources with ambiguous loss estimation formulas that can be based on insufficient or inaccurate information (Central Region Urban Environmental Improvement Project, CRUEIP, 2003; Chen et al., 2007; Oddo et al., 2018). Hence, in this study, we attempt to demonstrate that a standardized loss estimation method can still provide valuable information for flood damage prevention. The quality of the estimated flood-induced economic impact is influenced by the skill of FIER-estimated inundation extents that has been discussed in Section 5.1. Another factor is the accuracy of the DEM as the calculation of inundation depths relies on it as a topographic reference. The spatial resolution of FIER-estimated inundation extents can also play a role, especially in the LMRB floodplains with extremely low relief. Since the calculation of the inundation depths starts from extracting the elevations of inundation boundaries, a finer resolution inundation map can be helpful for extracting more accurate elevations along the inundation boundary. The spatial resolution of FIER-forecasted inundation extents can be tuned to be finer during the Sentinel-1 imagery retrieval from the GEE data catalog using RESTEE as Section 2.1 described. Finally, more detailed rice cultivation-related data, such as geospatial information of different rice varieties, and corresponding planting and harvesting calendars, if available, can further improve the accuracy of the estimated flood-induced rice economic losses.

The results here demonstrate the potential of FIER for rapidly forecasting the spatial distribution of flood-induced rice economic losses. While the post-event flood damage estimation has been done in many recent studies (Chung et al., 2019; Kwak et al., 2015; Oddo et al., 2018; Okazumi et al., 2014; Triet et al., 2018), FIER allows prompt pre-event forecasting of flood damages that can help decision-makers take timely proactive measures. Applications of FIER to rapidly forecast other flood-induced socio-economic damages, such as on infrastructure and households, are also possible with corresponding damage curves (Chen, 2007; Oddo et al., 2018).

5.3 Framework scalability

FIER is an innovative data-driven approach that produces inundation forecasts based on the correlation between the spatiotemporal patterns extracted from satellite imagery and external hydrological data. It is mathematically simple and has a high scalability, enabling us to relatively easily build and operate the framework for any flood-prone regions in the world with the cloud-based GEE data catalog which has archived the Sentinel-1 GRDH imagery over the globe that can be retrieved and preprocessed by the GEE-based Python APIs as Section 2.1 described. Moreover, a Python implementation of FIER, called FIERpy and developed by SCO (https://github.com/SERVIR/fierpy), can be run on Python-based cloud computing platforms, such as the Google Colaboratory (Google Colab). Hence, end-users that are interested in building their regional FIER framework but have rather limited computational resources can implement it on the cloud computing platforms. Considering the increasing flood risks worldwide (Tellman et al., 2021), the flexibility and scalability of FIER provide valued opportunities toward a rapid operational inundation forecasting system that can be relatively easily implemented over other flood-prone regions such as Bangladesh where in-situ and forecasted water levels can be obtained from the Bangladesh Water Development Board (BWDB) (http://www.ffwc.gov.bd/).

In addition, FIER has flexibility regarding the sources and types of the hydrological data used as inputs. The current FIER-Mekong system uses our in-house VIC model-aided satellite altimetry-based water level forecasting system (Chang et al., 2019) since the required water level forecasts at Can Tho are not provided by the operational water level forecasting system that MRC maintains (https://portal.mrcmekong.org/monitoring/flood-forecasting). However, MRC's water level forecasting system provides more accurate forecasts at the other three gauges (Kratie, Koh Khel, and Chau Doc), and therefore, it is possible to use both of the water level forecasting systems if such needs are identified from the end users. Moreover, not only water levels but streamflow data can be used to build the FIER framework. Thus, FIER can be integrated with natural streamflow obtained from a hydrologic model such as HYPE (Du et al., 2020) or VIC (Hossain et al., 2017), and/or regulated outflow from a reservoir obtained from, for example, the Reservoir Assessment Tool (RAT) (Biswas et al., 2021; Das et al., 2022) or the Integrated Reservoir Operation Scheme (IROS) (Du et al., 2022).

6 Conclusions and Future Scopes

This study has implemented FIER, a data-driven satellite imagery-based inundation extent forecasting framework, for the LMRB floodplains, where the implementation of the conventional approach is challenging. A rapid inundation extent forecasting system and a freely available user-friendly web application hosted by a cloud platform have been built as well. The system can rapidly generate daily continuous forecasts of inundation extents and depths with lead times up to 18 days which can be exported as GeoTIFF. The GeoTIFF files can be conveniently used for further geospatial analysis, such as combing with different land cover data for spatial prediction of flood-induced damages and economic losses.

Here, we generated FIER-forecasted inundation extents for the wet season of 2020 and 2021, and cross-compared them with inundation extents from the real Sentinel-1A images, to demonstrate its fairly promising skills. The error sources of forecasted inundation extents include the error in the input forecasted water levels, as well as the uncertainties in the FIER regression models that were possibly caused by human intervention of the floodplain water dynamics (e.g., with the dense network of dikes, sluice gate operation, water pumping). We also demonstrated an application of FIER-derived continuous forecasted inundation extents for spatial prediction of the flood-induced rice economic losses. Such spatial loss prediction can help decision-makers prioritize when and where proactive flood damage prevention measures should be taken. For instance, decision-makers can disseminate flood risk warnings to the inhabitants in the areas where rice paddies may be damaged by floods in the following days with severity information through Short Message Service (SMS) on mobile phones via local providers. After being informed, the local inhabitants can then evaluate the necessity to adjust the rice reaping schedule. For future work, the spatial flood-induced loss prediction will be made available on the web application, so decision-makers or any end-users that have an internet connection can directly obtain the results without processing the data on their own. Such an open web application can also help address the delays in flood warning dissemination caused by bureaucratic inefficiency since local inhabitants with internet access can get information directly from the web application on their own (Keoduangsine and Goodwin, 2012). Note that FIER-Mekong can also rapidly generate hindcasted inundation extents with historical water levels, which are also important for land-use planning and risk mapping (Oddo et al., 2018). The FIER-hindcasted inundation extents and rice economic losses for the year 2018, the most recent wet year, were also presented.

More importantly, with cloud-based databases, such as the GEE data catalog that archives the Sentinel-1 imagery over the globe, FIER has the potential to be easily implemented in other flood-prone regions in the world. FIER also has the flexibility to use forecasted water levels from different models, ensembling their strengths to generate more accurate forecasted inundation extents. An example is to combine the VIC model-aided satellite altimetry-based water level forecasting system used in this study with the MRC's operational forecasting system as Section 5.3 described. On the other hand, historical and forecasted natural and regulated streamflow obtained from hydrologic model and a reservoir operation scheme can be used as well to forecast inundation extents due to not only natural but regulated floods.

It is also worth mentioning that the types of satellite imagery that can be used for the FIER process are not restricted to SAR imagery. In fact, the use of both SAR and optical imagery through data fusion can help address the limitation of FIER. Since FIER forecasts the inundation extents based on spatiotemporal patterns of historical satellite images, the maximal inundation extents it can forecast are limited by the historical inundation extents that have been observed. As Sentinel-1A itself was launched in 2014 and has a 12-day revisiting cycle, some historical extreme flood events may be missing. Thus, the sole use of Sentinel-1A imagery may limit the forecasting capability of FIER. The optical imagery, on the other hand, have temporally longer and denser observations. Therefore, it is expected that combining SAR and optical imagery through data fusion techniques can help overcome the limitation of using a single source of satellite imagery.

Software availability

https://github.com/skd862/fier_mekong

Acknowledgements

This study is supported by NASA's Applied Sciences Program for SERVIR (80NSSC20K0152) and GEOGloWS (80NSSC18K0423).

References

Ahamed, A., Bolten, J.D., 2017. A MODIS-based automated flood monitoring system for southeast asia. Int. J. Appl. Earth Obs. Geoinf. 61, 104–117. https://doi.org/https://doi.org/10.1016/j.jag.2017.05.006

Balica, S., Dinh, Q., Popescu, I., Vo, T.Q., Pham, D.Q., 2014. Flood impact in the Mekong Delta, Vietnam. J. Maps 10, 257–268. https://doi.org/10.1080/17445647.2013.859636

Bates, P.D., De Roo, A.P.J., 2000. A simple raster-based model for flood inundation simulation. J. Hydrol. 236, 54–77. https://doi.org/https://doi.org/10.1016/S0022-1694(00)00278-X

Bates, P. D., Pappenberger, F., Romanowicz, R. J., 2014. Uncertainty in flood inundation modelling, in Beven, K. J., Hall, J. (Eds.), Applied Uncertainty Analysis for Flood Risk Management, Imperial College Press, 232 – 269

Bernhofen, M. V, Whyman, C., Trigg, M.A., Sleigh, P.A., Smith, A.M., Sampson, C.C., Yamazaki, D., Ward, P.J., Rudari, R., Pappenberger, F., Dottori, F., Salamon, P., Winsemius, H.C., 2018. A first collective validation of global fluvial flood models for major floods in Nigeria and Mozambique. Environ. Res. Lett. 13, 104007. https://doi.org/10.1088/1748-9326/aae014

Bich Tho, L.C., Umetsu, C., 2022. Sustainable farming techniques and farm size for rice smallholders in the Vietnamese Mekong Delta: A slack-based technical efficiency approach. Agric. Ecosyst. Environ. 326, 107775. https://doi.org/https://doi.org/10.1016/j.agee.2021.107775

Biswas, N., Hossain, F., Bonnema, M., Lee, H., Chishtie, F., 2021. Towards a global Reservoir Assessment Tool for predicting hydrologic impacts and operating patterns of exisiting and planned reservoirs, Environ. Model. Softw. 140. https://doi.org/10.1016/j.envsoft.2021.105043

Central Region Urban Environmental Improvement Project (CRUEIP), 2003. Supplementary Appendix [Resettlement plan]: Report and Recommendation of the President to the Board of Directors on a Proposed Loan to the Socialist Republic of Vietnam for the Central Region Urban Environmental Improvement Project, Asian Development Bank: Manila, Philippines.

Chang, C.-H., Lee, H., Hossain, F., Basnayake, S., Jayasinghe, S., Chishtie, F., Saah, D., Yu, H., Sothea, K., Du Bui, D., 2019. A model-aided satellite-altimetry-based flood forecasting system for the Mekong River. Environ. Model. Softw. 112, 112–127. https://doi.org/https://doi.org/10.1016/j.envsoft.2018.11.017

Chang, C.-H., Lee, H., Kim, D., Hwang, E., Hossain, F., Chishtie, F., Jayasinghe, S., Basnayake, S., 2020. Hindcast and forecast of daily inundation extents using satellite SAR and altimetry data with rotated empirical orthogonal function analysis: Case study in Tonle Sap Lake Floodplain. Remote Sens. Environ. 241, 111732. https://doi.org/https://doi.org/10.1016/j.rse.2020.111732

Cramb, R., Sareth, C., and Vuthy, T., 2020. The Commercialisation of Rice Farming in Cambodia, in Cramb, R. (Ed.), White Gold: The Commercialisation of Rice Farming in the Lower Mekong Basin, Palgrave Macmillan, 227 – 245

Chen, J., 2007. Flood damage map for the Huong River Basin: based on inundation depths, land use types and population density, using depth-damage curves, maximum damage values and depth-mortality curves. University of Twente, Enschede, Netherlands.

Chen, A., Giese, M., Chen, D., 2020. Flood impact on Mainland Southeast Asia between 1985 and 2018—The role of tropical cyclones. J. Flood Risk Manag. 13, e12598. https://doi.org/https://doi.org/10.1111/jfr3.12598

Chen, Z., Luo, J., Chen, N., Xu, R., Shen, G., 2019. RFim: A Real-Time Inundation Extent Model for Large Floodplains Based on Remote Sensing Big Data and Water Level Observations. Remote Sens. . https://doi.org/10.3390/rs11131585

Chung, S., Takeuchi, J., Fujihara, M., Oeurng, C., 2019. Flood damage assessment on rice crop in the Stung Sen River Basin of Cambodia. Paddy Water Environ. 17, 255–263. https://doi.org/10.1007/s10333-019-00718-1

Das, P., Hossain, F., Khan, S., Biswas, N. K., Lee, H., Piman, T., Meechaiya, C., Ghimire, U., Hosen, K., 2022. Reservoir Assessment Tool 2.0: Stakeholder driven improvements to satellite remote sensing based reservoir monitoring, Environ. Model. Softw. (In Review)

DeVries, B., Huang, C., Armston, J., Huang, W., Jones, J.W., Lang, M.W., 2020. Rapid and robust monitoring of flood events using Sentinel-1 and Landsat data on the Google Earth Engine. Remote Sens. Environ. 240, 111664. https://doi.org/https://doi.org/10.1016/j.rse.2020.111664

Du, T.L.T., Lee, H., Bui, D.D., Arheimer, B., Li, H.-Y., Olsson, J., Darby, S.E., Sheffield, J., Kim, D., Hwang, E., 2020. Streamflow prediction in “geopolitically ungauged” basins using satellite observations and regionalization at subcontinental scale. J. Hydrol. 588, 125016. https://doi.org/https://doi.org/10.1016/j.jhydrol.2020.125016

Du, T.L.T., Lee, H., Bui, D.D., Graham, L.P., Darby, S.D., Pechlivanidis, I.G., Leyland, J., Biswas, N.K., Choi, G., Batelaan, O., Bui, T.T.P., Do, S.K., Tran, T. V, Nguyen, H.T., Hwang, E., 2022. Streamflow Prediction in Highly Regulated, Transboundary Watersheds Using Multi-Basin Modeling and Remote Sensing Imagery. Water Resour. Res. 58, e2021WR031191. https://doi.org/https://doi.org/10.1029/2021WR031191

Dung, N. V, Merz, B., Bárdossy, A., Thang, T.D., Apel, H., 2011. Multi-objective automatic calibration of hydrodynamic models utilizing inundation maps and gauge data. Hydrol. Earth Syst. Sci. 15, 1339–1354. https://doi.org/10.5194/hess-15-1339-2011

Gilbert, G. K., 1884. Finley’s tornado predictions. Am. Meteorol. J. 1, 166 – 172.

Hansen, M.C., Potapov, P. V, Moore, R., Hancher, M., Turubanova, S.A., Tyukavina, A., Thau, D., Stehman, S. V, Goetz, S.J., Loveland, T.R., Kommareddy, A., Egorov, A., Chini, L., Justice, C.O., Townshend, J.R.G., 2013. High-Resolution Global Maps of 21st-Century Forest Cover Change. Science. 342, 850 LP – 853. https://doi.org/10.1126/science.1244693

Horton, A.J., Triet, N.V.K., Hoang, L.P., Heng, S., Hok, P., Chung, S., Koponen, J., Kummu, M., 2022. The Cambodian Mekong floodplain under future development plans and climate change. Nat. Hazards Earth Syst. Sci. 22, 967–983. https://doi.org/10.5194/nhess-22-967-2022

Hossain, F., Sikder, S., Biswas, N., Bonnema, M., Lee, H., Luong, N.D., Hiep, N.H., Du Duong, B., Long, D., 2017. Predicting Water Availability of the Regulated Mekong River Basin Using Satellite Observations and a Physical Model. Asian J. Water, Environ. Pollut. 14, 39–48. https://doi.org/10.3233/AJW-170024

Hung, N.N., Delgado, J.M., Güntner, A., Merz, B., Bárdossy, A., Apel, H., 2014. Sedimentation in the floodplains of the Mekong Delta, Vietnam Part II: deposition and erosion. Hydrol. Process. 28, 3145–3160. https://doi.org/https://doi.org/10.1002/hyp.9855

Hung, N.N., Delgado, J.M., Tri, V.K., Hung, L.M., Merz, B., Bárdossy, A., Apel, H., 2012. Floodplain hydrology of the mekong delta, Vietnam. Hydrol. Process. 26, 674–686. https://doi.org/10.1002/hyp.8183

Imani, M., You, R.-J., Kuo, C.-Y., 2014. Caspian Sea level prediction using satellite altimetry by artificial neural networks. Int. J. Environ. Sci. Technol. 11, 1035–1042. https://doi.org/10.1007/s13762-013-0287-z

Johnson, J.M., Munasinghe, D., Eyelade, D., Cohen, S., 2019. An integrated evaluation of the National Water Model (NWM)–Height Above Nearest Drainage (HAND) flood mapping methodology. Nat. Hazards Earth Syst. Sci. 19, 2405–2420. https://doi.org/10.5194/nhess-19-2405-2019

Kaiser, H.F., 1958. The varimax criterion for analytic rotation in factor analysis. Psychometrika 23, 187–200. https://doi.org/10.1007/BF02289233

Keoduangsine, S., Goodwin, R., 2012. An Appropriate Flood Warning System in the Context of Developing Countries. Int. J. Innov. Technol. Manag. 3.

Kim, D., Lee, H., Laraque, A., Tshimanga, R.M., Yuan, T., Jung, H.C., Beighley, E., Chang, C.H., 2017. Mapping spatio-temporal water level variations over the central congo river using palsar scansar and envisat altimetry data. Int. J. Remote Sens. 38, 7021–7040. https://doi.org/10.1080/01431161.2017.1371867

Kim, T., Yang, T., Gao, S., Zhang, L., Ding, Z., Wen, X., Gourley, J.J., Hong, Y., 2021. Can artificial intelligence and data-driven machine learning models match or even replace process-driven hydrologic models for streamflow simulation?: A case study of four watersheds with different hydro-climatic regions across the CONUS. J. Hydrol. 598, 126423. https://doi.org/https://doi.org/10.1016/j.jhydrol.2021.126423

Kohavi, R., Provost, F., 1998. Glossary of Terms. Mach. Learn. 30, 271–274. https://doi.org/10.1023/A:1017181826899

Kwak, Y., Arifuzzanman, B., Iwami, Y., 2015. Prompt Proxy Mapping of Flood Damaged Rice Fields Using MODIS-Derived Indices. Remote Sens. . https://doi.org/10.3390/rs71215805

Kien, N. V., Han, N. H., and Cramb, R., 2020. Trends in Rice-Based Farming Systems in the Mekong Delta, in Cramb, R. (Ed.), White Gold: The Commercialisation of Rice Farming in the Lower Mekong Basin, Palgrave Macmillan, 347 – 373

Leandro, J., Chen, A.S., Schumann, A., 2014. A 2D parallel diffusive wave model for floodplain inundation with variable time step (P-DWave). J. Hydrol. 517, 250–259. https://doi.org/https://doi.org/10.1016/j.jhydrol.2014.05.020

Lee, H., Yuan, T., Jung, H.C., Beighley, E., 2015. Mapping wetland water depths over the central Congo Basin using PALSAR ScanSAR, Envisat altimetry, and MODIS VCF data. Remote Sens. Environ. 159, 70–79. https://doi.org/https://doi.org/10.1016/j.rse.2014.11.030

Lorenz, E. N., 1956. Empirical Orthogonal Functions and Statistical Weather Prediction. Statistical Forecasting Project Scientific Report No. 1., Massachusetts Institute of Technology, Cambridge, MA, U.S.

Lopes, A., Nezry, E., Touzi, R. and Laur, H., 1990. Maximum a posteriori speckle filtering and first order texture models in SAR images. 10th Annual International Symposium on Geoscience and Remote Sensing, 2409-2412, doi: 10.1109/IGARSS.1990.689026.

Maitah, K., Smutka, L., Sahatqija, J., Maitah, M., Phuong Anh, N., 2020. Rice as a Determinant of Vietnamese Economic Sustainability. Sustain. . https://doi.org/10.3390/su12125123

Markert, K.N., Markert, A.M., Mayer, T., Nauman, C., Haag, A., Poortinga, A., Bhandari, B., Thwal, N.S., Kunlamai, T., Chishtie, F., Kwant, M., Phongsapan, K., Clinton, N., Towashiraporn, P., Saah, D., 2020. Comparing Sentinel-1 Surface Water Mapping Algorithms and Radiometric Terrain Correction Processing in Southeast Asia Utilizing Google Earth Engine. Remote Sens. . https://doi.org/10.3390/rs12152469

Matsubara, T., Truong, C.T., Le, C.D., Kitaya, Y., Maeda, Y., 2020. Transition of Agricultural Mechanization, Agricultural Economy, Government Policy and Environmental Movement Related to Rice Production in the Mekong Delta, Vietnam after 2010. AgriEngineering . https://doi.org/10.3390/agriengineering2040043

Moriasi, D.N., Arnold, J.G., Van Liew, M.W., Bingner, R.L., Harmel, R.D., Veith, T.L., 2007. Model evaluation guidelines for systematic quantification of accuracy in watershed simulations. Trans. ASABE 50, 885–900.

MRC, 2005. Overview of the Hydrology of the Mekong Basin, Mekong River Commission. Vientiane. https://doi.org/1728 3248

MRC, 2009. Flood Damages, Benefits and Flood risk in Focal Areas: The Flood Management and Mitigation Programme, Component 2: Structural Measures and Flood Proofing in the Lower Mekong Basin. Draft Report, Vol 2C.

MRC, 2011. Basin Development Plan Programme, Planning Atlas of the Lower Mekong River Basin. Phnom Penh, Cambodia.

MRC, 2021. Mekong Low Flow and Drought Conditions in 2019 – 2021, Hydrological

Conditions in the Lower Mekong River Basin. Vientiane, Lao PDR.

Nobre, A.D., Cuartas, L.A., Hodnett, M., Rennó, C.D., Rodrigues, G., Silveira, A., Waterloo, M., Saleska, S., 2011. Height Above the Nearest Drainage – a hydrologically relevant new terrain model. J. Hydrol. 404, 13–29. https://doi.org/https://doi.org/10.1016/j.jhydrol.2011.03.051

Nobre, A.D., Cuartas, L.A., Momo, M.R., Severo, D.L., Pinheiro, A., Nobre, C.A., 2016. HAND contour: A new proxy predictor of inundation extent. Hydrol. Process. 30, 320–333. https://doi.org/10.1002/hyp.10581

Oddo, P.C., Ahamed, A., Bolten, J.D., 2018. Socioeconomic Impact Evaluation for Near Real-Time Flood Detection in the Lower Mekong River Basin. Hydrol. . https://doi.org/10.3390/hydrology5020023

Okazumi, T., Tanaka, S., Kwak, Y., Shrestha, B.B., Sugiura, A., 2014. Flood vulnerability assessment in the light of rice cultivation characteristics in Mekong River flood plain in Cambodia. Paddy Water Environ. 12, 275–286. https://doi.org/10.1007/s10333-013-0403-1

Pagano, T.C., 2014. Evaluation of Mekong River commission operational flood forecasts, 2000-2012. Hydrol. Earth Syst. Sci. 18, 2645–2656. https://doi.org/10.5194/hess-18-2645-2014

Peter, B.G., Cohen, S., Lucey, R., Munasinghe, D., Raney, A., Brakenridge, G.R., 2022. Google Earth Engine Implementation of the Floodwater Depth Estimation Tool (FwDET-GEE) for Rapid and Large Scale Flood Analysis. IEEE Geosci. Remote Sens. Lett. 19, 1–5. https://doi.org/10.1109/LGRS.2020.3031190

Pokhrel, Y., Shin, S., Lin, Z., Yamazaki, D., Qi, J., 2018. Potential Disruption of Flood Dynamics in the Lower Mekong River Basin Due to Upstream Flow Regulation. Sci. Rep. 8, 1–13. https://doi.org/10.1038/s41598-018-35823-4

Simard, M., Pinto, N., Fisher, J.B., Baccini, A., 2011. Mapping forest canopy height globally with spaceborne lidar. J. Geophys. Res. Biogeosciences 116. https://doi.org/10.1029/2011JG001708

Smith, L.C., 1997. Satellite remote sensing of river inundation area, stage, and discharge: a review. Hydrol. Process. 11, 1427–1439. https://doi.org/10.1002/(SICI)1099-1085(199708)11:10<1427::AID-HYP473>3.0.CO;2-S

Tellman, B., Sullivan, J.A., Kuhn, C., Kettner, A.J., Doyle, C.S., Brakenridge, G.R., Erickson, T.A., Slayback, D.A., 2021. Satellite imaging reveals increased proportion of population exposed to floods. Nature 596, 80–86. https://doi.org/10.1038/s41586-021-03695-w

Teng, J., Jakeman, A.J., Vaze, J., Croke, B.F.W., Dutta, D., Kim, S., 2017. Flood inundation modelling: A review of methods, recent advances and uncertainty analysis. Environ. Model. Softw. 90, 201–216. https://doi.org/10.1016/j.envsoft.2017.01.006

Triet, N.V.K., Dung, N.V., Hoang, L.P., Duy, N. Le, Tran, D.D., Anh, T.T., Kummu, M., Merz, B., Apel, H., 2020. Future projections of flood dynamics in the Vietnamese Mekong Delta. Sci. Total Environ. 742, 140596. https://doi.org/https://doi.org/10.1016/j.scitotenv.2020.140596

Triet, N.V.K., Dung, N. V, Merz, B., Apel, H., 2018. Towards risk-based flood management in highly productive paddy rice cultivation – concept development and application to the Mekong Delta. Nat. Hazards Earth Syst. Sci. 18, 2859–2876. https://doi.org/10.5194/nhess-18-2859-2018

Try, S., Tanaka, S., Tanaka, K., Sayama, T., Hu, M., Sok, T., Oeurng, C., 2020a. Projection of extreme flood inundation in the Mekong River basin under 4K increasing scenario using large ensemble climate data. Hydrol. Process. 34, 4350–4364. https://doi.org/https://doi.org/10.1002/hyp.13859

Try, S., Tanaka, S., Tanaka, K., Sayama, T., Lee, G., Oeurng, C., 2020b. Assessing the effects of climate change on flood inundation in the lower Mekong Basin using high-resolution AGCM outputs. Prog. Earth Planet. Sci. 7, 34. https://doi.org/10.1186/s40645-020-00353-z

Twele, A., Cao, W., Plank, S., Martinis, S., 2016. Sentinel-1-based flood mapping: a fully automated processing chain. Int. J. Remote Sens. 37, 2990–3004. https://doi.org/10.1080/01431161.2016.1192304

Vu, H. T. D., Vu, H. L., Oberle, P., Andreas, S., Nguyen, P C., Tran, D. D., 2022. Datasets of land use change and flood dynamics in the Vietnamese Mekong Delta. Data Br., 42, 108268. https://doi.org/10.1016/j.dib.2022.108268

Wing, O.E.J., Bates, P.D., Sampson, C.C., Smith, A.M., Johnson, K.A., Erickson, T.A., 2017. Validation of a 30 m resolution flood hazard model of the conterminous United States. Water Resour. Res. 53, 7968–7986. https://doi.org/10.1002/2017WR020917

Wing, O.E.J., Sampson, C.C., Bates, P.D., Quinn, N., Smith, A.M., Neal, J.C., 2019. A flood inundation forecast of Hurricane Harvey using a continental-scale 2D hydrodynamic model. J. Hydrol. X 4, 100039. https://doi.org/https://doi.org/10.1016/j.hydroa.2019.100039

Yamazaki, D., Ikeshima, D., Tawatari, R., Yamaguchi, T., O'Loughlin, F., Neal, J.C., Sampson, C.C., Kanae, S., Bates, P.D., 2017. A high-accuracy map of global terrain elevations. Geophys. Res. Lett. 44, 5844–5853. https://doi.org/10.1002/2017GL072874

Zheng, X., Maidment, D.R., Tarboton, D.G., Liu, Y.Y., Passalacqua, P., 2018. GeoFlood: Large-Scale Flood Inundation Mapping Based on High-Resolution Terrain Analysis. Water Resour. Res. 54, 10,10-13,33. https://doi.org/https://doi.org/10.1029/2018WR023457

Zhou, T., Wang, F., Yang, Z., 2017. Comparative Analysis of ANN and SVM Models Combined with Wavelet Preprocess for Groundwater Depth Prediction. Water . https://doi.org/10.3390/w9100781

Declaration of interests

☐The authors declare that they have no known competing financial interests or personal relationships that could have appeared to influence the work reported in this paper.

☒The authors declare the following financial interests/personal relationships which may be considered as potential competing interests:

Hyongki Lee reports financial support was provided by NASA. Chi-Hung Chang reports financial support was provided by NASA.